Magnetic tracking for catheterization procedure, using giant-magnetoresistance and space-varying magnetic field free point

L. Paquet, A. Solignac, K. Tse Ve Koon, M. Ohta, N. Tsuruoka, Y. Haga, C. Fermon, M. Pannetier-Lecoeur, B. Ducharne

Magnetic tracking for catheterization procedure, using giant-magnetoresistance and space-varying magnetic field free point

L. Paquet[1,2,3,4], A. Solignac[5], K. Tse Ve Koon[2], M. Ohta[3,4], N. Tsuruoka[6], Y. Haga[4,6], C. Fermon[5], M. Pannetier-Lecoeur[5], B. Ducharne[1,7]

[1] ELyTMaX IRL3757, Univ Lyon, INSA Lyon, Centrale Lyon, Université Claude Bernard Lyon 1, Tohoku University, Sendai 980-8577, Japan.
[2] CREATIS, Université Lyon1, CNRS UMR5220, INSERM U1206, INSA-Lyon, 69621 Villeurbanne, France.
[3] Institute of Fluid Science, Tohoku University, 2-1-1, Katahira, Aoba-ku, Sendai, Miyagi 980-8577, Japan.
[4] Graduate School of Biomedical Engineering, Tohoku University, 6-6 Aramaki-Aza-Aoba, Aoba-ku, Sendai, Miyagi 980-8579, Japan.
[5] SPEC, CEA, CNRS, Université Paris-Saclay, CEA Saclay, 91191 Gif-sur-Yvette, France.
[6] Graduate School of Engineering, Tohoku University 6-6 Aramaki Aza Aoba, Aoba-ku, Sendai, Miyagi 980-8579, Japan.
[7] Univ Lyon, INSA Lyon, LGEF EA682, 69621 Villeurbanne, France

ABSTRACT

X-ray fluoroscopic imaging is the standard method for obtaining catheter position and monitoring the patient's vascular network during catheterization procedures. However, this method exposes both patients and doctors to ionizing radiation. To address this issue, we propose an alternative method for tracking the catheter inside the human body by integrating a magnetic sensor at the catheter tip and generating a known magnetic field (MF) around the operative zone. The catheter's position can then be determined by measuring this MF.

Due to the mandatory small size of the catheter, we utilized giant-magnetoresistance (GMR) sensors for this tracking system. GMR sensors require only two wires for connection, have a wide bandwidth that allows flexibility in selecting the working frequency and can detect low-intensity MFs down to the nano Tesla range.

Our method is based on the time detection of a moving null MF, known as the Field-Free Point (FFP) for MF generation. This approach requires only a single sensor smaller than 300 μm^2, making it suitable for any catheter. We constructed an experimental setup to demonstrate the feasibility of this method in one dimension and obtained promising performance results.

KEYWORDS

Magnetic tracking, catheter position assessment, micrometric magnetic sensor.

HIGHLIGHTS

- A method based on magnetic particle imaging is adapted to track a catheter
- Small sized giant magnetoresistors are integrated into a catheter
- An experimental setup is built to show the tracking feasibility in 1D

I - INTRODUCTION

Catheterization is a minimally invasive surgery used for various diagnostic and therapeutic purposes [1]. These procedures typically involve a small incision (1 to 3 mm, according to [2]), do not always require general anesthesia, and can be fast to perform, among other advantages [3]. With the help of a contrast agent opaque to X-rays, doctors can get a 2D image showing the catheter inside the patient's blood vessel. For example, it can detect potential aneurysms and assess the patient's vascular network condition. Medical professionals treat aneurysms through different procedures, including coiling or stent placement [4], all carried out through an inserted catheter.

Although catheterization has seen extensive development, there remains room for improvement [5]. Despite careful dosage and protective equipment, X-rays still raise safety concerns due to ionizing radiation exposure for both patients and medical staff, particularly

during long procedures. Additionally, practitioners must rely on a 2D image showing a projection of the 3D arteria, which can impede navigation [5, 6]. In clinical use, the position of the catheter must be known with good precision and in real-time [7]. Hence, time and spatial resolutions are critical specifications of catheter tracking systems [8]. X-ray fluoroscopy performs significantly well with a spatial precision below 1 mm and an image at around 24 Hz sampling frequency, creating real-time visualization. X-ray imaging is a mature technology, and its characteristics will be challenging to overcome. Nonetheless, they give a baseline for comparison.

However, X-ray fluoroscopy is not without its limitations, including the associated radiation risks and the need for injection of contrast agents, which are not suitable for all patients, especially those with kidney deficiencies. The magnetic tracking (M-tracking) system developed in this study does not directly compete with X-rays but could be a contributing imaging method to improve overall vascular treatment. In this regard, besides a lesser spatial or temporal resolution, the M-tracking shows many other advantages. One key advantage is that M-tracking eliminates ionizing radiation, reducing potential risks, particularly in procedures requiring prolonged exposure. For example, it could reduce the dose of contrast agents for kidney-deficient patients [9]. Moreover, M-tracking's ability to operate without continuous X-ray use can offer added safety, potentially decreasing cumulative radiation exposure for both patients and clinicians. From a long-term perspective, the M-tracking could be a first step toward a non-radiative imaging method. However, obtaining an image of the vascular network and overlaying the catheter's position will be necessary, which may be challenging, particularly due to breathing movements.

Regarding the Magnetic Field (MF) generation and waveform, there are different approaches to obtaining a position from a magnetic measurement. A known method is to find the position of the sensor by optimizing the unknown position and orientation in the three directions of space, denoted (x, y, z, α, β, γ), so the measured field matches the calculation for those positions. Examples of such system can be found in [10] or [11] and usually requires 3 orthogonals sensors. The MF encodes the volume with a nearly bijective relationship between positions and MF measurements. Our system is different; it was inspired by the magnetic particle imaging (MPI) setup described in [12]. If the Magnetic Field (MF) can be zero at a unique position called Field Free Point (FFP) at a given time, and if this FFP can move throughout the whole volume, then knowing when the sensor measures the FFP would indicate its position. Therefore, a time-varying MF with an FFP covering the entire volume must be built to make such tracking possible. This work's novelty relies on the single magnetic sensor and the tracking routine. Indeed, to our knowledge, only few magnetic tracking uses a GMR sensor such in [13], even though the possibility has been mentioned [14]. Most of other application use coils or commercially avalaible Hall-effect sensor [15]. GMR sensors are highly sensitive and can detect low-intensity MFs, including static fields, over a wide frequency range. Their small size (tens of micrometers) facilitates miniaturization, even for the most minor catheters with diameters as small as 300 µm.

Using MF with a sensor inside a catheter requires a small and precise sensor. GMR sensors are well-suited for this purpose, being extremely compact and capable of detecting low-intensity fields. Their wide bandwidth allows for adaptation to the clinical environment, particularly in noisy settings such as clinical rooms. This paper demonstrates that in a 1D configuration, the GMR

and the innovative tracking algorithm are useful for determining the sensor's location. The achieved time and spatial resolutions provide a baseline for future improvements and the transition to 2D and 3D configurations.

II – GIANT MAGNETO-RESISTANCE SENSOR

GMRs are composed of multiple thin layers, including two ferromagnetic films separated by a non-magnetic metallic spacer, with a total active thickness typically less than 30 nm. These layers are deposited on a silicon substrate (around 300 µm thick), which can be thinned down if necessary [16, 17]. Table 1 shows the detailed composition of a typical GMR sensor and the thickness of each layer.

Table. 1 – GMR typical layers' composition and thickness in nm [13].

Layer composition	Ta	NiFe	CoFe	Cu	CoFe	Ru	CoFe	IrMn	Ru	Ta
Layer thickness (nm)	3	5	2.1	2.3	2.1	0.85	2	6	0.4	5

GMRs have a wide frequency range and can even operate under static MF. They can detect low-intensity fields in the nano Tesla range [18]. These characteristics make them suitable candidates for our applications. The first ferromagnetic layer, known as the reference (or fixed) layer, acts as a permanent magnet. The second ferromagnetic layer, called the free (or unfixed) layer, is magnetically soft and changes its magnetization in response to external magnetic fields. These changes lead to fluctuations in overall resistance due to the spin-dependent charge transport phenomenon [19].

The shape anisotropy of the free layer determines the GMR's linearity. At rest, without an external field, the angle between the reference and the free layers' orientation is 90°. When a field is applied in the plane of the stack, the angle can decrease to 0°, reducing the resistance accordingly. When an opposite field is applied, the angle increases to 180°, and the resistance increases.

In Fig. 1, we first characterized the GMR used in this study using Helmholtz coils [20, 21]. We monitored the evolution of the resistance vs. MF (R(MF), Fig. 1a). Then, we implemented it in a Wheatstone bridge (Fig. 1c). The voltage drop across the bridge for different levels of applied MF was recorded (Fig. 1b). Where $\mathrm{V_{out}(MF)} = \Delta\mathrm{R(MF)} \cdot \mathrm{I_{in}}$, $\Delta\mathrm{R}$ is the GMR resistance variation, and $\mathrm{I_{in}}$ the Wheatstone bridge imposed input current. The Helmholtz coils create a precise and easy-to-control magnetic field in the volume where the sensor is positioned, allowing us to obtain the typical response curve. The orientation angle between the reference and the free layers is almost at its maximum for a field of -2.5 mT and its minimum for 2.5 mT. Between these values, the change in resistance follows a quasi-linear trend. This field window constitutes the working range where the GMR behaves as a magnetic sensor. The Wheatstone bridge (Fig. 1c) enhances sensitivity and accuracy in detecting the small resistance changes of the GMR by suppressing the resistance offset of each element and some possible thermal drift. The chip in the bottom part of Fig. 1a includes four integrated Wheatstone bridges. Due to its prominent electrical contacts, it is

easier to manipulate in the laboratory. Since it integrates the same GMR as those implemented in the catheter, we used it for most of the experimental results reported in this work.

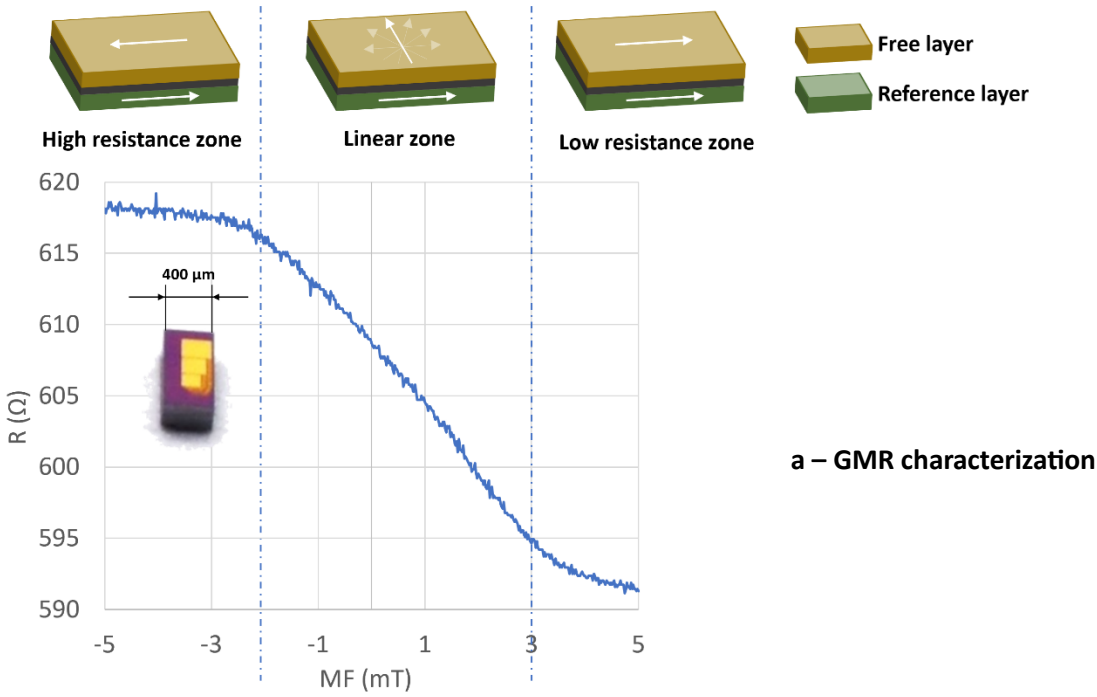

a – GMR characterization

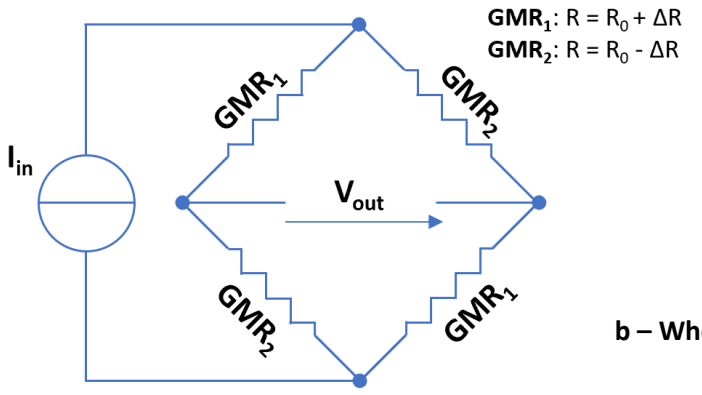

b – Wheatsone bridge

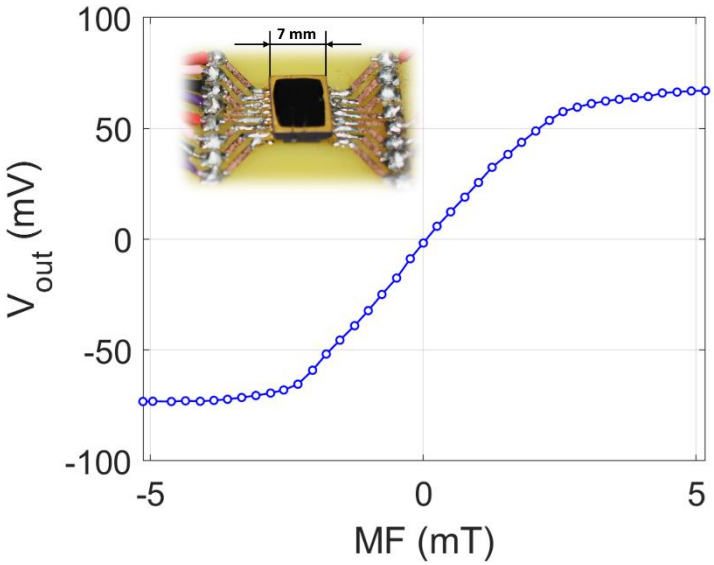

c – Wheatsone bridge characterization

Fig. 1a – Resistance of the GMR vs. an external magnetic field. The top sketches show the corresponding ferromagnetic layers' magnetic orientations. **Fig. 1b** – GMRs plugged in a Wheatstone bridge configuration. **Fig. 1c** – Output voltage V_{out} along the Wheatstone bridge supplied with a current source of I_{in} = 1 mA for the typical GMR used in this study vs. an in-plane external magnetic field (MF).

GMR sensors offer long-term stability due to their solid-state nature, which eliminates moving parts and reduces the risk of mechanical failure. Their operation based on spin-dependent electron transport is highly stable, ensuring consistent performance over time. Furthermore, their resilience to environmental fluctuations such as temperature changes and electromagnetic interference adds to their reliability, making them particularly suitable for clinical applications where precision and durability are essential.

When compared to other magnetic sensor technologies, GMR sensors offer a compelling combination of advantages for catheter tracking. Unlike Hall-effect sensors, which are robust but lack the sensitivity required to detect weak magnetic fields, GMR sensors can operate in the nano-Tesla range, making them ideal for precise applications. While anisotropic magnetoresistance (AMR) sensors offer better sensitivity than Hall sensors, they still fall short of the performance of GMR in detecting low-intensity magnetic fields. Tunneling magnetoresistance (TMR) sensors, though comparable in sensitivity to GMR, are more complex and require additional wiring, which can be cumbersome for catheterization procedures. GMR sensors strike a balance between high sensitivity, minimal wiring, and low power consumption, making them particularly suited for space-constrained environments such as medical catheters.

II – INSTRUMENTED CATHETER

The integration of GMR sensors is a significant challenge in this work. The catheters we target can have an outer diameter as small as 300 µm, as seen in neurovascular applications [22]. Typical commercially available GMRs are too bulky to be integrated into a catheter. Therefore, additional GMRs have been designed with integration in mind, making them small enough for catheter integration. Fig. 2a depicts a photograph of the prepared chips, and Fig. 2b provides a detailed description and the dimensions.

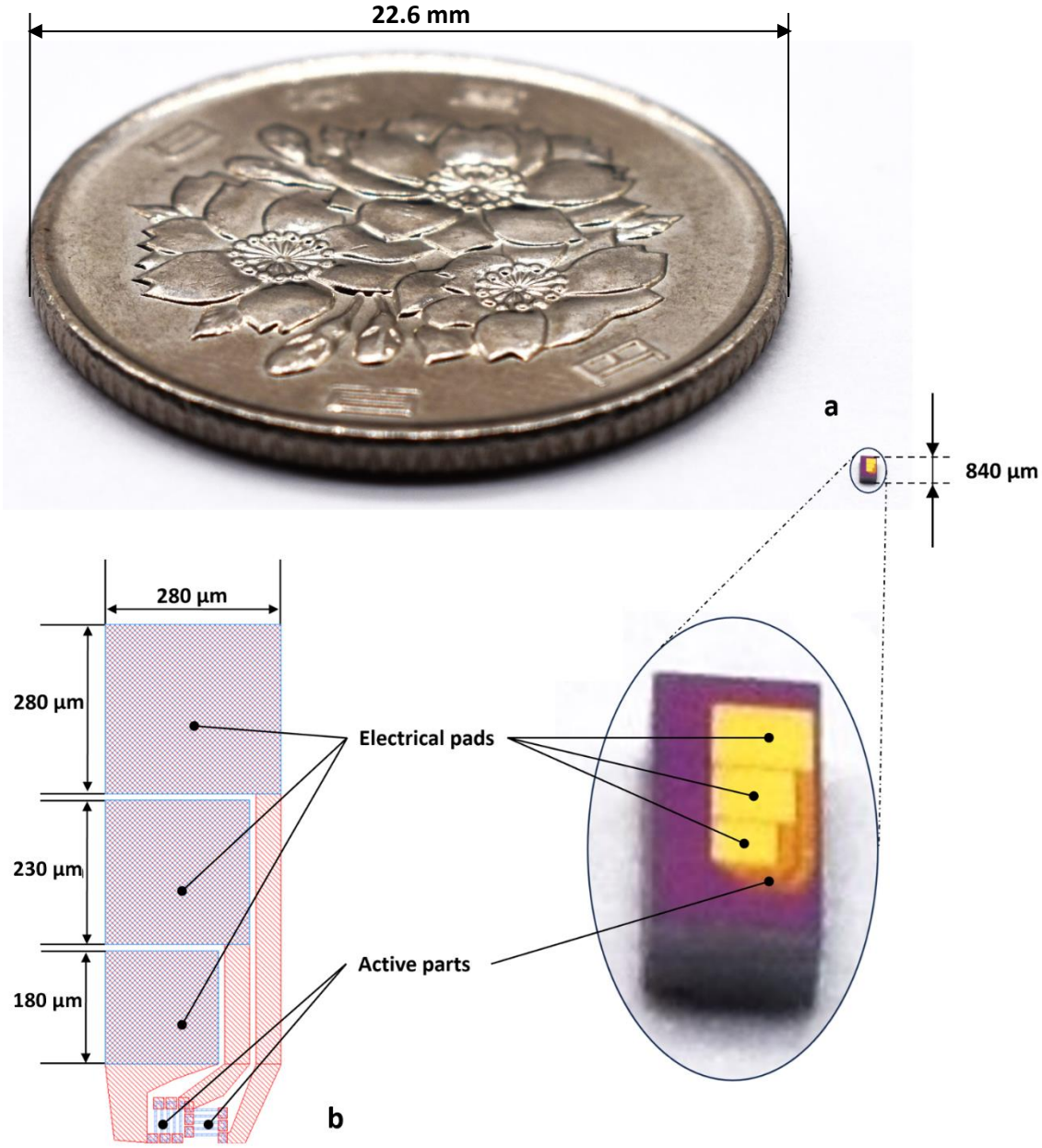

Fig. 2a – Picture of the GMR chip. **Fig. 2b** – Description and dimensions of a typical GMR chip designed for integration on the catheter.

Each chip contained two orthogonally arranged GMR sensors, designed to measure magnetic fields in two directions for potential 2D tracking applications. While this study focused on using a single sensor for one-dimensional measurements, the same chip can be leveraged in future work to perform additional 2D tracking tests, demonstrating the versatility of the GMR configuration. The most prominent parts of the chip are the connection pads, which range from 180 x 180 µm² to 280 x 280 µm², whereas the active area occupies less than 100 µm² for the two GMRs. The chip shape and size provide a degree of freedom that can be adjusted when necessary.

As a preliminary proof of concept, we mounted a 300 x 700 µm sensor chip onto a catheter with a 1.5 mm outer diameter. We achieved it by welding the GMR to a flexible gold strip PCB, which included three gold strips. Each GMR pad was wire-bonded to a gold strip using gold wire. The catheter's existing wires were soldered on the other end of the gold strips to ensure the electrical connections. Finally, we covered each part with epoxy for protection. Fig. 3 depicts the resulting instrumented catheter. Having the sensor at the catheter tip is critical for delivering precise positional information, still at this study stage and for convenience, we positioned the sensor two centimeters away from the catheter tip rather than at the tip itself, meaning the measured position will not correspond exactly to the tip position.

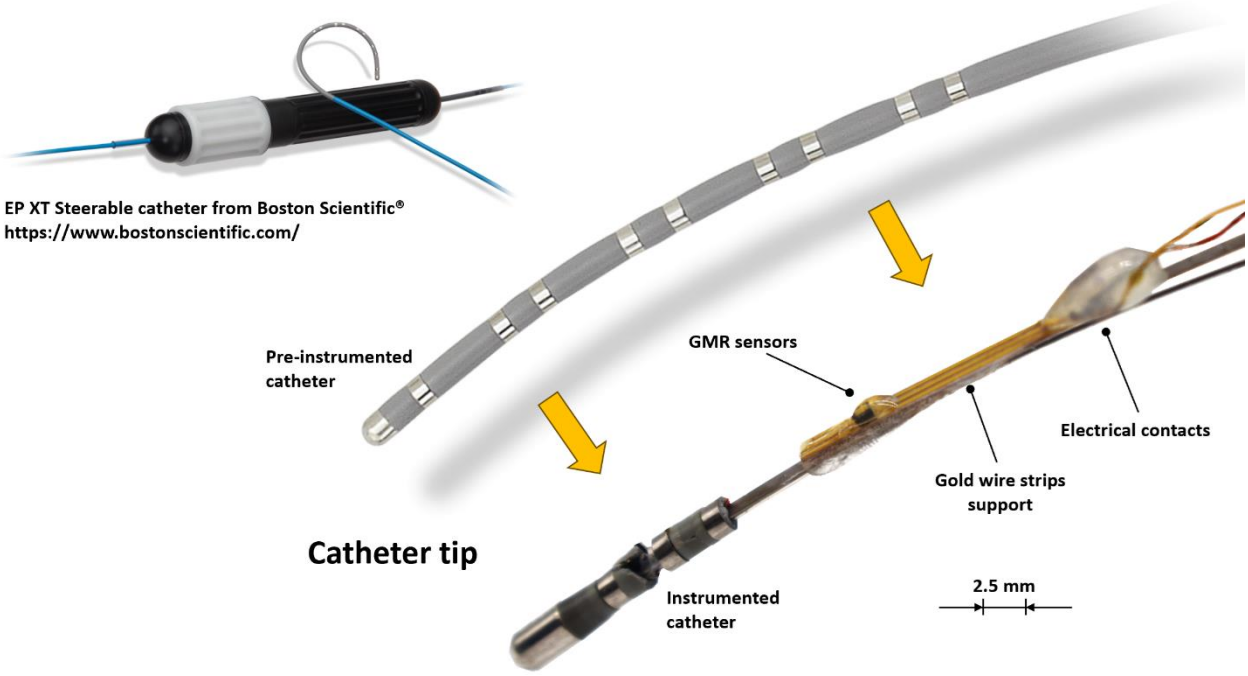

Fig. 3 – Instrumented catheter, including the GMR sensor and the electrical contacts.

Our custom-made GMR sensors offer several advantages over commercial alternatives, particularly in size and performance customization. Their significantly smaller dimensionsmake them ideal for integration at the catheter tip. Also, our sensors are specifically tailored for catheter tracking applications, allowing for the fine-tuning of their magnetic response to match the experimental conditions.

III – TRACKING POSITION ALGORITHM

Most existing MF-tracking technologies rely on multiple sensors, each sensitive to one spatial axis. For example, the method described in [10] or [13] combines three sensors. By generating a known static field and measuring its three spatial components, it is possible to fully determine the sensors' position (x, y, z) and orientation (α, β, γ). Most other solutions described in the scientific literature are based on the same principles but use different sensor technologies (coils

in [23, 24]) or methods to generate the Magnetic Field (MF) (eight emitting coils in [25], or a planar field generator in [26]).

The method proposed here differs in the MF generation and how to determine the sensor and, therefore, catheter position. It could theoretically reduce the number of sensors needed to only one, significantly decreasing the required size and the complexity of the catheter manufacturing. However, it increases the setup complexity. A time-varying MF is created instead of a static MF and is used to compute the sensor's position. This MF is null at a unique point in space called the Field Free Point (FFP). The FFP moves over time inside the working volume. At any given time step, there is a unique FFP. Searching when the GMR sensor detects the FFP allows us to estimate its position accurately.

This method was inspired by solutions found in the magnetic particle imaging (MPI) framework, where the working volume is swept with an FFP to obtain the local concentration measurements of magnetic nanoparticles [8][27]. The magnetic response from the particles is typically measured via pick-up coils. The FFP method in MPI involves creating a region with no magnetic field, surrounded by areas with high magnetic field gradients. When superparamagnetic nanoparticles are introduced into the body, they align with the magnetic field. By scanning the FFP across the region of interest, MPI detects how the nanoparticles respond to the changing magnetic fields. This data is then processed to reconstruct a detailed image, highlighting the distribution of nanoparticles and providing insights into physiological and pathological conditions [28-30].

In our study, the GMR sensor replaces the superparamagnetic particles. Moving the FFP inside the operation volume [31] can be done through several methods. The MF induced by a current flowing through a single circular coil, offset from the center by O_z, can be expressed analytically (Eq. 1). In one dimension, considering the field along the rotation axis of the coil, the B_z component is given by:

$$B_z = \frac{\mu_0 a^2}{2} \cdot \left[\frac{iN}{(a^2+(z+O_z)^2)^{3/2}} \right] \quad (1)$$

Where i is the current flowing through the coil, N is its number of turns, a its radius, and μ_0 the vacuum permeability. This formula corresponds to a coil with its rotation axis along the z-axis, as illustrated in Fig. 4 below.

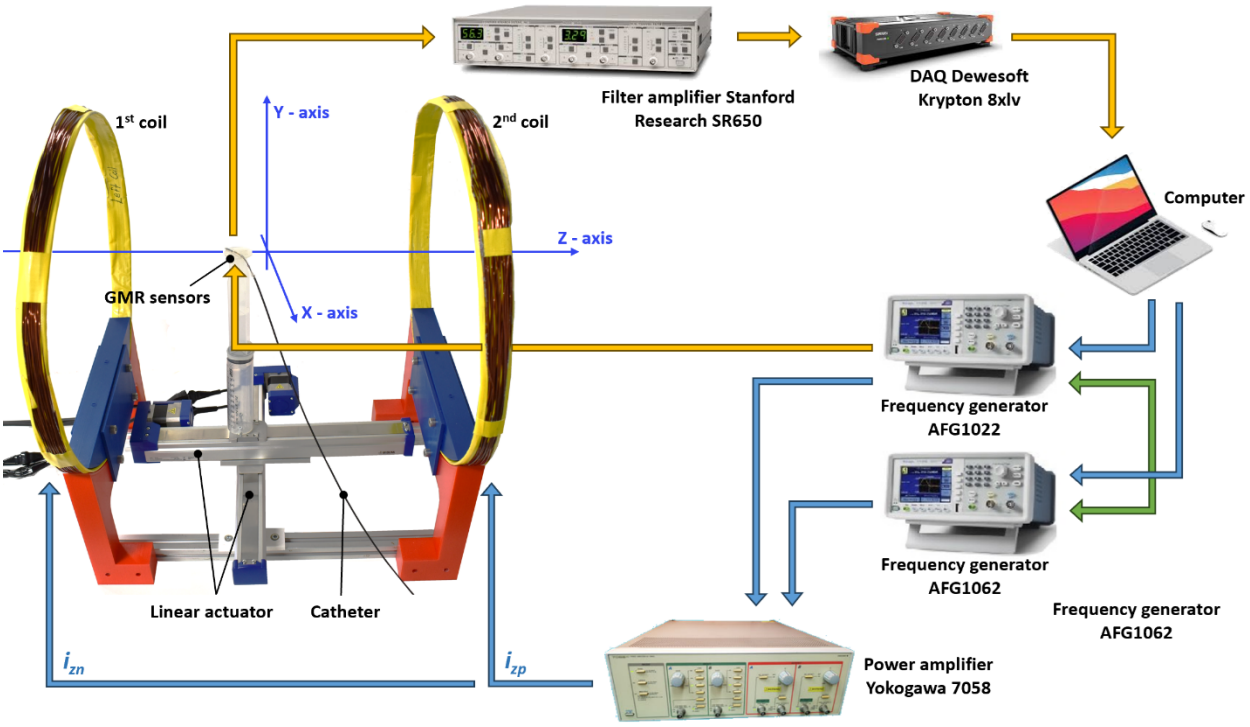

Fig. 4 – Schematic and photo of the 1D experimental setup.

If another similar coil is positioned at the offset $-O_z$ position and two electrical currents, i_{zp} and i_{zn} flow through them, B_z is equal to the addition of the field induced by each coil (Eq. 2):

$$B_z = \frac{\mu_0 a^2}{2} \cdot \left[\frac{i_{zp} N}{(a^2+(z+O_z)^2)^{3/2}} + \frac{i_{zn} N}{(a^2+(z-O_z)^2)^{3/2}} \right] \quad (2)$$

Setting the middle of the coils as $z = 0$ induces an opposite spatial offset +/- O_z. Eq. 2 depends solely on the electrical currents and the z position, as the radius and the offset distance are known values. When an opposite current is applied to each loop ($i_{zp} = -i_{zn}$), B_z is zero at the position z = 0. This FFP is unique on the z-axis and for this combination of currents.

There is a single ratio of currents leading to an FFP for each position. In higher dimensions (2D or 3D), with two coils, more zeros would appear, but only one would remain on the z-axis when B_x and B_y are zero. Fig. 5 shows three profiles. Each current ratio creates a unique FFP at a different position. It is possible to supply both coils with carefully chosen currents varying over time so the FFP moves along the z-axis in the zone separating the excitation coils. Numerous possible current input functions lead to a moving FFP [32]. The differences between them will be in the speed, acceleration, and trajectory of the FFP. These functions will likely impact the system's performance and will be investigated carefully in the following sections of this work.

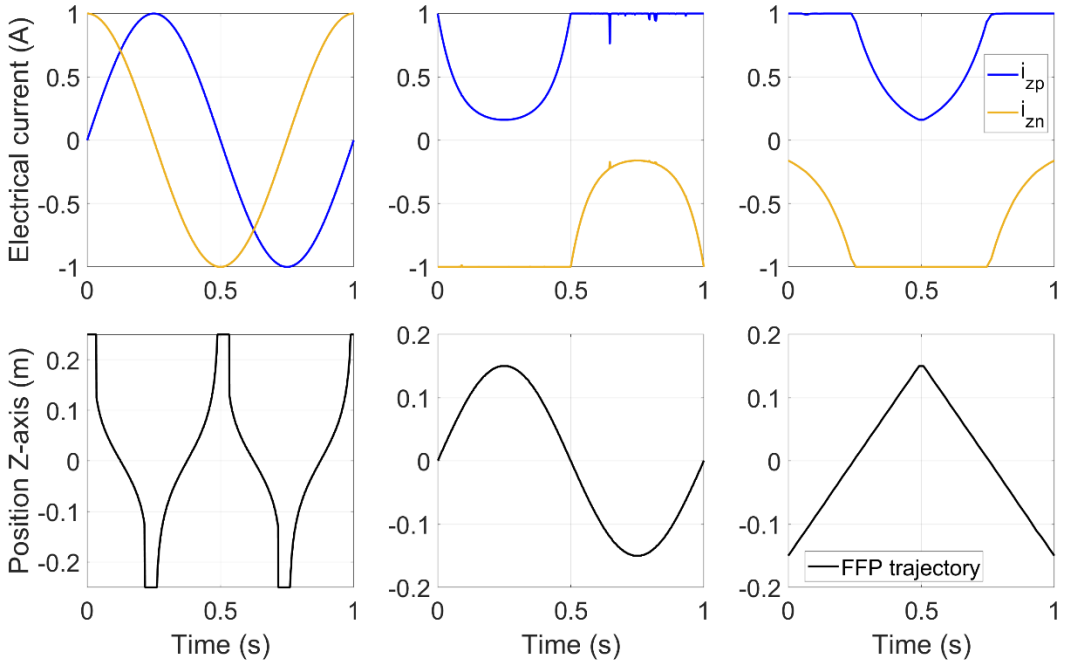

Fig. 5 – Electrical currents i_{zp} and i_{zn} in the excitation coils and their corresponding FFP trajectory below.

When the coils are supplied with specific currents, the GMR sensor detects the FFP at a particular time. This timing depends on the sensor's position. One advantage of this method is that it works with a single sensor. Conversely, because the angles are unknown, measuring a non-zero value would not enable determining the position. Considering a sensor in a random orientation (α, β, γ), its measured signal depends on the magnetic field vector description (B_x, B_y, B_z) and the angle of the sensor, such as $B_x \sin(\alpha) + B_y \sin(\beta) + B_z \sin(\gamma)$. This expression confirms that it is impossible to determine the component or angle with a single measurement.

Now, if in a unique position, $|B| = \sqrt{B_x^2 + B_y^2 + B_z^2} = 0$, the sensor will measure this null Magnetic Field (MF) independently of its angle. Hence, measuring a zero implies that every component is equal to zero. A zero could still be obtained when the magnetic vector is perfectly orthogonal to the sensor. Still, this situation is unlikely to happen, and using the sensor's previous position can help correct the error.

A time-dependent FFP position function FFP(t) = (x, y, z) can be defined by describing the position of the FFP over time. The measurement is worth zero when the sensor and the FFP are in the same position, thus giving the sensor position at different instants. The time it takes for the FFP to scan the whole volume gives the rate of position acquisition, hence temporal resolution. The current supplied to the coils and the position function are directly linked. In Fig. 5, three different position functions (bottom row) and their respective current (top row) are shown in a single-dimension configuration. Those functions can be obtained by calculating the MF, B_z and searching the position of the zero for an arbitrary current ratio, as used to compute the sinusoidal

current (Left-hand-side plots in Fig. 5). The other way is to arbitrarily decide the position of the zero and optimize the currents via an optimization algorithm using SciPy python module. The second method was used to compute the currents for the sinusoidal (middle plots) and triangular position functions (right-hand-side plots). Because the optimization is not always perfect, some outliers can be seen in Fig. 5 when computing the current for the sinusoidal position function. The current peaks could be removed without changing the FFP trajectory.

IV – EXPERIMENTAL RESULTS

4.1 Experimental setup

An experimental setup, schematically described in Fig. 4, was built, including two excitation coils with a radius of 23 cm and 30 turns of 3 mm diameter copper wire. We determined the radius and number of turns based on MF simulations. One significant characteristic of the field under consideration was the field's spatial derivative; a steeper profile results in a more precise zero-crossing. The spatial resolution is directly affected by the sensor's selectivity. With a distance of 50 cm between the coils, the generated field should be sufficient to achieve a spatial resolution of 1 mm using our sensor.

The coils were driven by amplified, modulated sinusoidal currents produced by two separate Tektronix (Beaverton, Oregon, USA) frequency generators, AFG1062 and AFG1022, for the right and left coils, respectively. We achieved the signal synchronization using the synchronization output of the first generator. We accomplished the voltage amplification using a Yokogawa (Tokyo, Japan) 7058 power amplifier set to a gain of 10. The AFG1022 frequency generator also provided the sensor with a 500 Hz sinusoidal signal at 3 V peak-to-peak through its secondary channel.

The sensing was performed using the GMR sensor described in sections 2 and 3. This sensor was mounted on a Misumi (Tokyo, Japan) RS102 translation stage, allowing movement over a 30 cm range along the common axis of the coils, as shown in Fig. 3, ensuring precise positioning. The voltage drop across the GMR sensor was filtered and amplified using a Stanford Research (Sunnyvale, California, USA) SR650 filter. Signal acquisition was carried out with a DEWEsoft (Trbovlje, Slovenia) Krypton 8xLV acquisition system at a sampling frequency of 20 kHz.

4.2 Acquisition

We supplied the GMR sensor and the coils with alternating waveforms to enable signal extraction using a digital lock-in amplifier [33]. This method efficiently eliminates unwanted frequency components from the signal and amplifies the relevant ones. The Wheatstone bridge signal contains multiple frequency components, and the objective is to isolate the specific component that carries the desired information. The signal under test is multiplied by both a sine and a cosine wave at the same frequency as the target component. This operation results in two new signals: one with a static component and another at twice the original frequency. By applying a low-pass filter (LPF) to remove the alternating component and retaining only the static

component for both signals, it is possible to extract the amplitude of the target component and determine its phase difference relative to the reference sine and cosine signals. Below is the mathematical description of the lock-in amplifier process, assuming a pure sinusoidal input signal. This signal is multiplied by the sine and cosine wave at the same frequency:

$$\begin{cases} A_O \sin(2\pi f \mathrm{t} + \phi)\cos(2\pi f \mathrm{t}) = \frac{A_O}{2}\sin(4\pi f \mathrm{t} + \phi) + \frac{A_O}{2}\sin(\phi) \\ A_O \sin(2\pi f \mathrm{t} + \phi)\sin(2\pi f \mathrm{t}) = \frac{A_O}{2}\cos(4\pi f \mathrm{t} + \phi) + \frac{A_O}{2}\cos(\phi) \end{cases} \quad (3)$$

With A_0 the amplitude of the signal under test, f its frequency, and ϕ its phase. By assuming a perfect low-pass filter, we reduce the signals to:

$$\begin{cases} X = \frac{A_O}{2}\sin(\phi) \\ Y = \frac{A_O}{2}\cos(\phi) \end{cases} \quad (4)$$

By using the two above components, we can express the phase and the amplitude:

$$\begin{cases} \sqrt{X^2 + Y^2} = \sqrt{\left(\frac{A_0}{2}\sin(\phi)\right)^2 + \left(\frac{A_0}{2}\cos(\phi)\right)^2} = \sqrt{\left(\frac{A_0}{2}\right)^2 (\sin(\phi)^2 + \cos(\phi)^2)} = \sqrt{\left(\frac{A_0}{2}\right)^2} = \frac{A_0}{2} \\ \arctan\left(\frac{X}{Y}\right) = \arctan\left(\frac{\frac{A_0}{2}\sin(\phi)}{\frac{A_0}{2}\cos(\phi)}\right) = \arctan(\tan(\phi)) = \phi \end{cases} \quad (5)$$

The GMR sensor response depends upon the supplied voltage and the coils' magnetic field (MF). The resulting voltage drop across the GMR can theoretically be described as follows:

$$V_{out} = \Delta R \cdot I_{in} \quad (6)$$

$$V_{out} = \Delta R I_0 \sin(2\pi f_{se} \mathrm{t}) \quad (7)$$

$$V_{out} = Se\mu_0 H_0 \sin(2\pi f_c \mathrm{t} + \phi) I_0 \sin(2\pi f_{se} \mathrm{t}) \quad (8)$$

Using the product to sum trigonometric identities:

$$V_{out} = \frac{Se\mu_0 H_0}{2}\cos(2\pi(f_c - f_{se}) + \phi) - \frac{Se\mu_0 H_0}{2}\cos(2\pi(f_c + f_{se}) + \phi) \quad (9)$$

Where f_{se} and f_c are the signal frequency in the sensor and the coils, in this work, we set them to 500 Hz and 425 Hz, respectively. Se represents the sensor sensitivity, i.e., the variation of the resistance of the GMR vs. the applied magnetic field. The additive frequency component, $f_{se} + f_c$ = 925 Hz, was extracted with a numerical lock-in amplifier to return the magnetic field amplitude. Eq. 6 is only valid for a constant field H_0, corresponding to constant electrical currents in the coils. However, H_0 must change vs. time for the FFP to move. Therefore, the currents are amplitude-modulated signals with the envelope frequency chosen to be $f_p = 30mHz$ producing the FFP movement and the carrier at $f_c = 425Hz$ transmitting the information. Those currents are shown in Fig. 6a, with the corresponding FFP trajectory induced in Fig. 6b. The sensor was moved from +/- 15 cm along the z-axis to evaluate the setup performance, with 1 cm step increments and a total of q = 31 points. The sensor remained in the same position for 120 seconds, including 20 seconds of transient regime (stabilization of the lock-in amplifier) and 100 seconds of acquisition. The final result was the average of the signal over the acquisition period. This approach improves

the spatial resolution at the cost of the temporal resolution. In this study, to prove the feasibility of the tracking method, we decided to emphasize spatial resolution rather than temporal one.

Determining the position, even at a low rate, might prove helpful in performing discrete position checks during the procedure. However, measuring a position with too much uncertainty is not practical, regardless of the image refresh rate. During the 100-second acquisition, we measured the position six times to evaluate the variability. Since the sensor remains stationary during this time, the variability should be minimal, and the measured position should align with the actual position.

4.3 Results

Fig. 7 shows the first results using the position function displayed in Fig. 6b. The function links the time corresponding to the FFP measurement to a given position. The plotted result corresponds to the average value obtained over the six measurements for each position. The variability (+/- one standard deviation) below 1 mm is too small to be visible in this plot. The orange dotted line is the target. This first result (Fig. 7) leads to an average standard deviation for the complete trajectory (31 positions) of 0.993 mm, reaching a spatial resolution below 1 mm.

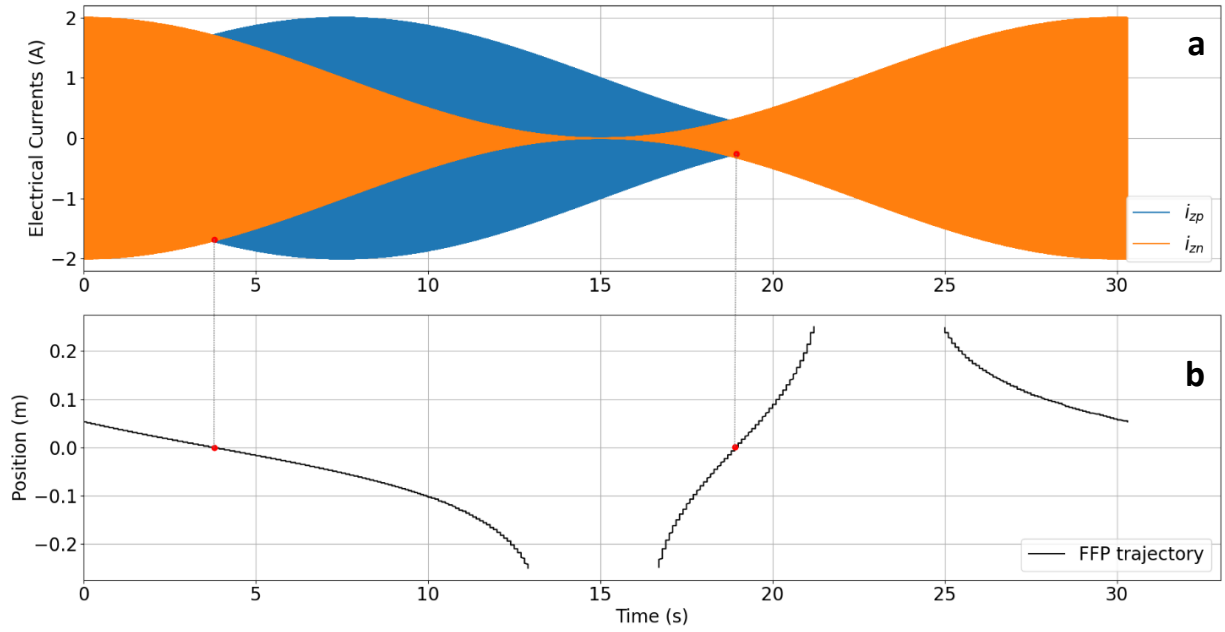

Fig. 6a – Electrical current in the excitation coils (i_{zp}, i_{zn}) modulated through a sinusoidal wave.
Fig. 6b – Corresponding time-dependent positioning function used to return the position. When modulated currents are equals, the FFP is at 0m, middle position of the coils as shown with the dotted line.

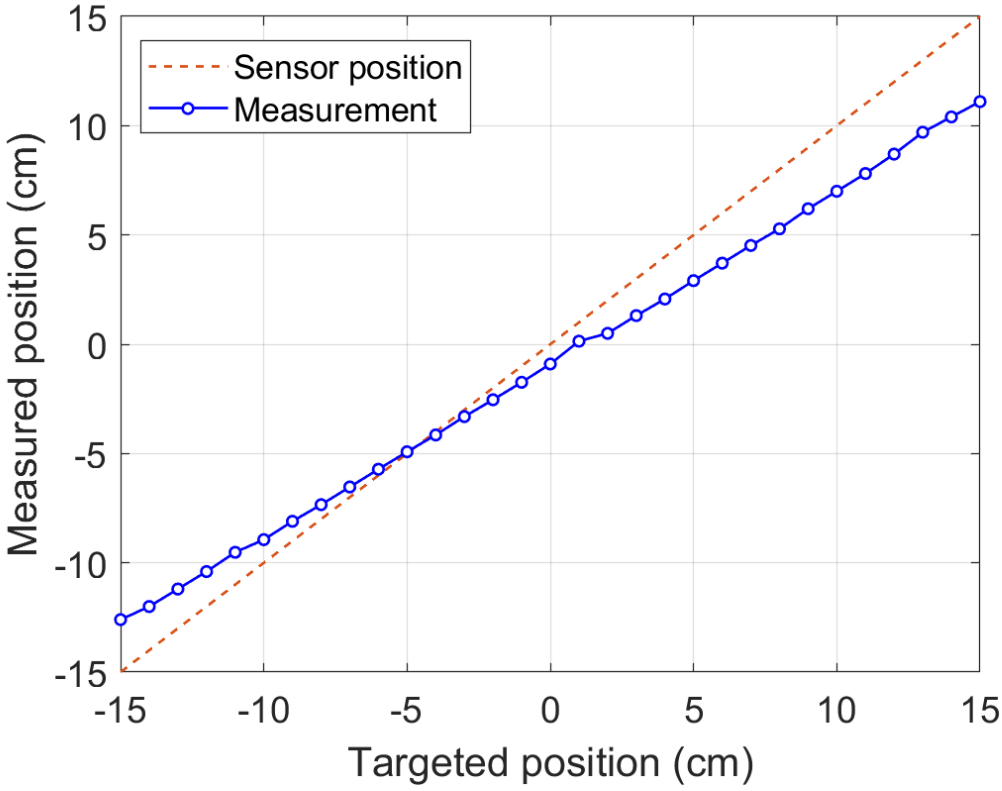

Fig. 7 – Comparison between the targeted and experimental positions measured with a lock-in low-pass filter time constant of τ = 1s for a 100 s acquisition time and after a 20 s transient phase.

The resulting error for this test calculated based on the relative Euclidean distance criteria (RED%) defined in Eq. 10 [34] gave 27.9 %:

$$\mathrm{RED}(\%) = \frac{100}{q} \cdot \sum_{i=1}^{q} \frac{\sqrt{\left(\mathrm{Position}_{\mathrm{exp}_i} - \mathrm{Position}_{\mathrm{targ}_i}\right)^2}}{\sqrt{\left(\mathrm{Position}_{\mathrm{targ}_i}\right)^2}} \tag{10}$$

However, we can observe a linear deviation in the experimental results of Fig. 7. This issue might come from an error in the position function (Fig. 6b) after the data acquisition. A minimum RED(%) could have been expected at the zero position with increasing errors on each side since the field derivative should be highest at zero and decrease as one moves towards the coils. This phenomenon, although present, displays an offset to the position of -5 cm. An asymmetry in the currents inside the coils could explain this. Therefore, we applied a linear correction to the function to solve it. As long as the error is consistent, we can use such a correction to achieve better positioning accuracy. The correction was computed by changing the amplitude of the position function and adding a shift as described in Eq. 11:

$$\mathrm{Correction}(\delta) = A\delta + B \tag{11}$$

Where δ is the position, A and B are constants set to 1.3 and 0.009, respectively.

Once the correction was applied, we plotted the newly measured position (see Fig. 8); this new set of experimental results reached a promising average RED(%) of 4.89 %. The correction greatly reduced the error but at a small cost of precision as the average standard deviation increased to 1.3 mm.

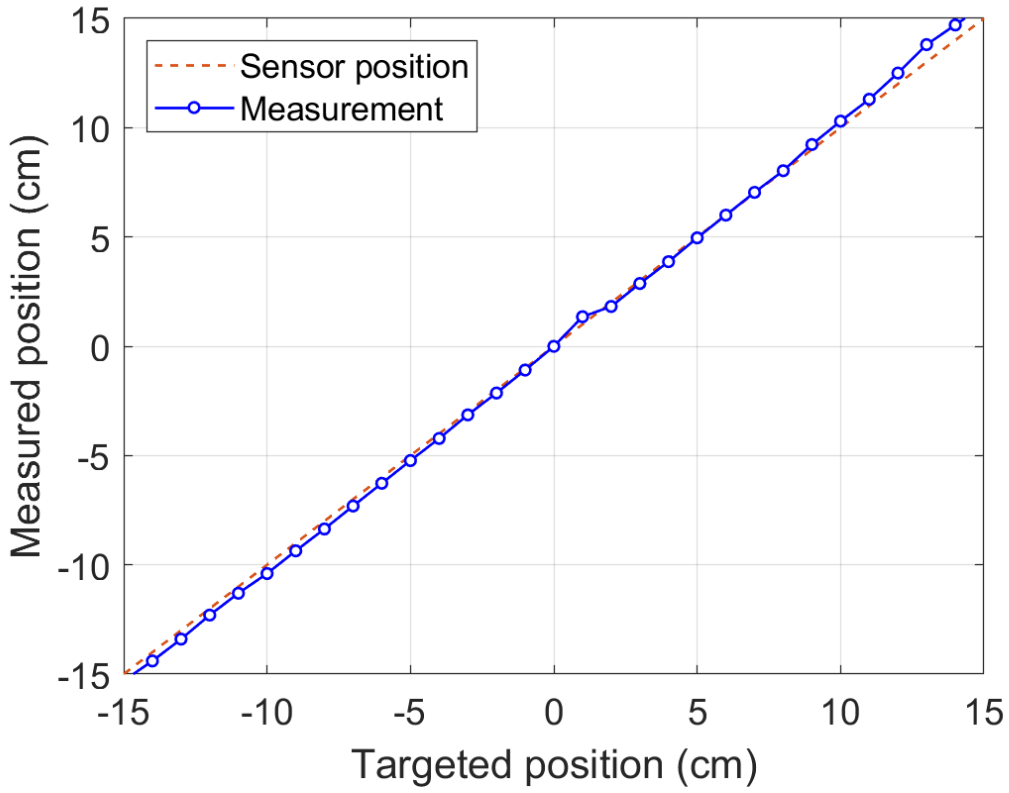

Fig. 8 – Comparison between the targeted and experimental positions after correction.

V – CONCLUSION

In this study, we proposed and verified the feasibility of an innovative method for tracking catheter position using a giant-magnetoresistance (GMR) sensor integrated within the catheter tip. By generating a known magnetic field (MF) and utilizing the time detection of a moving Field-Free Point (FFP), we established a system capable of precise catheter localization without ionizing radiation.

Our experimental results, limited to a one-dimensional setup, demonstrated promising accuracy and spatial resolution, achieving a standard deviation between 1.3 mm and 0.993 mm with or without post-processing corrections. These performances align with the 1 mm goal for vascular imaging and tracking applications. GMR sensors, known for their high sensitivity and small size, proved advantageous for miniaturization and integration into catheters with diameters as small as 300 µm. We assembled a homemade catheter associated with a GMR

sensor, demonstrating the integration possibilities. Further miniaturization is possible, and potential studies will focus on further size reduction.

Although our method currently focuses on spatial resolution, our findings indicate potential for further refinement and optimization to enhance both spatial and temporal resolution. Future work will aim to transition from 1D to 2D and 3D configurations, explore more complex position functions, and implement error correction mechanisms to improve positioning accuracy. The current method relies on filtration, which limits the acquisition speed but reduces noise, and we will study the balance between speed and noise reduction in higher-dimensional setups.

We also acknowledge the influence of external magnetic fields, including the Earth's magnetic field, as well as potential interference from the human body. Future experiments will include a calibration stage to correct for the Earth's magnetic field, ensuring accurate tracking. Although the human body generates weak magnetic fields (typically 10–100 pT), we do not anticipate significant interference with the catheter tracking system, given that our setup operates at much higher field strengths (around 1 mT). Should further interference be detected, we will explore the use of magnetic shielding to mitigate external noise.

Looking forward, we also plan to address the challenge of programming the FFP trajectory and potentially integrating vascular maps into the tracking system. While the current design does not synchronize with predefined vascular networks, future work could explore dynamic FFP control based on patient-specific anatomy, enhancing the precision of catheter navigation. The addition of such vascular mapping would further support real-time decision-making during procedures and provide an essential complement to X-ray fluoroscopy, potentially reducing radiation exposure and improving safety in complex vascular environments.

Additionally, the incorporation of a feedback mechanism could improve tracking speed and accuracy as we expand into multi-dimensional tracking. Preliminary tests have demonstrated that higher acquisition rates are key to achieving real-time adjustments, and optimizing the FFP trajectory will further enhance the feedback-controlled tracking system. We will continue refining these mechanisms to ensure optimal performance in 2D and 3D tracking scenarios.

In conclusion, the proposed magnetic tracking system represents a significant step toward safer, more precise catheterization procedures, reducing reliance on ionizing radiation and potentially enhancing the overall effectiveness of vascular treatments. The adaptability and sensitivity of the GMR sensor, combined with the innovative FFP tracking method and future improvements in both feedback mechanisms and vascular mapping, offer a promising avenue for continued research and clinical applications.

References

[1] Davidson, C.J. and Bonow, R.O., 1997. Cardiac catheterization. *Libby P*, *10*, p.18.

[2] Pancholy, S.B., Joshi, P., Shah, S., Rao, S.V., Bertrand, O.F. and Patel, T.M., 2015. Effect of vascular access site choice on radiation exposure during coronary angiography: the REVERE trial (Randomized Evaluation of Vascular Entry Site and Radiation Exposure). *JACC: Cardiovascular Interventions*, *8*(9), pp.1189-1196.

[3] Fu, Y., Liu, H., Huang, W., Wang, S. and Liang, Z., 2009. Steerable catheters in minimally invasive vascular surgery. *The International Journal of Medical Robotics and Computer Assisted Surgery*, *5*(4), pp.381-391.

[4] Shapiro, M., Becske, T., Sahlein, D., Babb, J. and Nelson, P.K., 2012. Stent-supported aneurysm coiling: a literature survey of treatment and follow-up. *American journal of neuroradiology*, *33*(1), pp.159-163.

[5] Kern, M.J., Sorajja, P. and Lim, M.J., 2015. *Cardiac catheterization handbook*. Elsevier Health Sciences.

[6] McFadden, S.L., Mooney, R.B. and Shepherd, P.H., 2002. X-ray dose and associated risks from radiofrequency catheter ablation procedures. *The British journal of radiology*, *75*(891), pp.253-265.

[7] Wutke, R., Lang, W., Fellner, C., Janka, R., Denzel, C., Lell, M., Bautz, W. and Fellner, F.A., 2002. High-resolution, contrast-enhanced magnetic resonance angiography with elliptical centric k-space ordering of supra-aortic arteries compared with selective X-ray angiography. *Stroke*, *33*(6), pp.1522-1529.

[8] Poulin, E., Racine, E., Binnekamp, D. and Beaulieu, L., 2015. Fast, automatic, and accurate catheter reconstruction in HDR brachytherapy using an electromagnetic 3D tracking system. *Medical physics*, *42*(3), pp.1227-1232.

[9] Aghamir, S.M.K., 2021. Successful retrograde intrarenal surgery (RIRS) for a 2-centimeter stone in a chronic renal failure (CRF) patient. *International Journal of Surgery Case Reports*, *87*, p.106375.

[10] Jaeger, H.A., Franz, A.M., O'Donoghue, K., Seitel, A., Trauzettel, F., Maier-Hein, L. and Cantillon-Murphy, P., 2017. Anser EMT: the first open-source electromagnetic tracking platform for image-guided interventions. *International journal of computer assisted radiology and surgery*, *12*, pp.1059-1067.

[11] Tanase, D., Goosen, J.F.L., Trimp, P.J., French, P.J., 2002. Multi-parameter sensor system with intravascular navigation for catheter/guide wire application. Sensors and Actuators A: Physical 97–98, 116–124.

[12] Gleich, B. and Weizenecker, J., 2005. Tomographic imaging using the nonlinear response of magnetic particles. *Nature*, *435*(7046), pp.1214-1217.

[13] Totsu, K., Haga, Y., Esashi, M., 2004. Three-axis magneto-impedance effect sensor system for detecting position and orientation of catheter tip. Sensors and Actuators A: Physical 111, 304–309.

[14] Schneider, M., Cormedics Corp, 2000. *Measuring position and orientation using magnetic fields*. U.S. Patent 6,073,043.

[15] Wu, X., Hou, W., Peng, C., Zheng, X., Fang, X., He, J., 2008. Wearable magnetic locating and tracking system for MEMS medical capsule. Sensors and Actuators A: Physical 141, 432–439.

[16] Chopin, C., Torrejon, J., Solignac, A., Fermon, C., Jendritza, P., Fries, P. and Pannetier-Lecoeur, M., 2020. Magnetoresistive sensor in two-dimension on a 25 µm thick silicon substrate for in vivo neuronal measurements. *ACS sensors*, *5*(11), pp.3493-3500.

[17] Kouakeuo, S.H.N., Solignac, A., Sabariego, R.V., Morel, L., Raulet, M.A., Toutsop, B., Tsafack, P. and Ducharne, B., 2022. Internal characterization of magnetic cores, comparison to finite element simulations:

a route for dimensioning and condition monitoring. *IEEE Transactions on Instrumentation and Measurement*, *71*, pp.1-10.

[18] Moulin, J., Doll, A., Paul, E., Pannetier-Lecoeur, M., Fermon, C., Sergeeva-Chollet, N. and Solignac, A., 2019. Optimizing magnetoresistive sensor signal-to-noise via pinning field tuning. *Applied Physics Letters*, *115*(12).

[19] Moulin, J., 2020. *Magnetic scanning probe microscope integrating magnetoresistive nanosensors* (Doctoral dissertation, Université Paris-Saclay).

[20] Trout, S.R., 1988. Use of Helmholtz coils for magnetic measurements. *IEEE Transactions on Magnetics*, *24*(4), pp.2108-2111.

[21] Saqib, M., Francis, S.N. and Francis, J.N., 2020, March. Design and development of Helmholtz coils for magnetic field. In *2020 International Youth Conference on Radio Electronics, Electrical and Power Engineering (REEPE)* (pp. 1-5). IEEE.

[22] Merz, C.T., 2021. Neurovascular Catheter Measurement System Development for Process and Design Effect Evaluation.

[23] O'Donoghue, K., Eustace, D., Griffiths, J., O'Shea, M., Power, T., Mansfield, H. and Cantillon-Murphy, P., 2014. Catheter position tracking system using planar magnetics and closed loop current control. *IEEE Transactions on Magnetics*, *50*(7), pp.1-9.

[24] Rasche, V., Holz, D., Köhler, J., Proksa, R. and Röschmann, P., 1997. Catheter tracking using continuous radial MRI. *Magnetic resonance in medicine*, *37*(6), pp.963-968.

[25] Li, M., Bien, T. and Rose, G., 2013. FPGA based electromagnetic tracking system for fast catheter navigation. *Int. J. Sci. Eng. Res*, *4*(9), pp.2566-2570.

[26] Knopp, T., Biederer, S., Sattel, T.F., Rahmer, J., Weizenecker, J., Gleich, B., Borgert, J. and Buzug, T.M., 2010. 2D model-based reconstruction for magnetic particle imaging. *Medical physics*, *37*(2), pp.485-491.

[27] Top, C.B., Güngör, A., Ilbey, S. and Güven, H.E., 2019. Trajectory analysis for field free line magnetic particle imaging. *Medical Physics*, *46*(4), pp.1592-1607.

[28] Gleich, B. and Weizenecker, J., 2005. Tomographic imaging using the nonlinear response of magnetic particles. *Nature*, *435*(7046), pp.1214-1217.

[29] Weizenecker, J., Gleich, B. and Borgert, J., 2008. Magnetic particle imaging using a field free line. *Journal of Physics D: Applied Physics*, *41*(10), p.105009.

[30] Goodwill, P.W., Saritas, E.U., Croft, L.R., Kim, T.N., Krishnan, K.M., Schaffer, D.V. and Conolly, S.M., 2012. X-space MPI: magnetic nanoparticles for safe medical imaging. *Advanced materials*, *24*(28), pp.3870-3877.

[31] Knopp, T., Biederer, S., Sattel, T., Weizenecker, J., Gleich, B., Borgert, J. and Buzug, T.M., 2008. Trajectory analysis for magnetic particle imaging. *Physics in Medicine & Biology*, *54*(2), p.385.

[32] Weizenecker, J., Borgert, J. and Gleich, B., 2007. A simulation study on the resolution and sensitivity of magnetic particle imaging. *Physics in Medicine & Biology*, *52*(21), p.6363.

[33] De Graaf, G. and Wolffenbuttel, R.F., 2012, May. Lock-in amplifier techniques for low-frequency modulated sensor applications. In *2012 IEEE International Instrumentation and Measurement Technology Conference Proceedings* (pp. 1745-1749). IEEE.

[34] Fagan, P., Ducharne, B., Zurek, S., Domenjoud, M., Skarlatos, A., Daniel, L. and Reboud, C., 2022. Iterative methods for waveform control in magnetic measurement systems. *IEEE Transactions on Instrumentation and Measurement*, *71*, pp.1-13.